Nuclear Science and Techniques (2026) 37:125
https://doi.org/10.1007/s41365-026-01911-8

Monte Carlo simulation of the focusing effect of a tapered glass capillary used in MeV-SIMS on heavy-ion beam with MeV-range energy

Ji-Wei Lai[1] · Tong-Tong Zhu[1] · Ming-Ming Yu[1] · Yun-Peng Cao[1] · Hong-Wen Cao[1] · Yi-Han Wang[1] · Kun Zhang[1]

Received: 17 July 2024 / Revised: 20 September 2024 / Accepted: 28 September 2024 / Published online: 16 April 2026

Abstract
Time-of-flight secondary-ion mass spectrometry (TOF-SIMS) is a powerful molecular imaging tool used in biomedical research. To overcome the low yield of non-fragmented molecular ions obtained by conventional (keV) SIMS, a novel SIMS method using MeV heavy primary ions (MeV-SIMS) has gained increasing scientific attention in recent years. We intend to develop an MeV-SIMS setup with a capillary microprobe system based on the 3 MV tandem accelerator as the first MeV-SIMS system in China. Instead of conventional magnetic or electrostatic lenses, a tapered glass capillary is used to collimate the ion beam in this device. To verify the feasibility of collimating or focusing MeV heavy ions using this capillary, understanding the main physical behaviors of MeV heavy ions interacting with the capillary is crucial. In this study, a Monte Carlo simulation program based on the Stopping and Range of Ions in Matter software is developed. The calculated energies and trajectories of heavy ions (e.g., I ions) are less affected by scattering, and both the scattered ions and recoil atoms ejected from the capillary are well separated from the direct beam in the target area. Under multiple scatterings, the contribution of the first scattering predominates. These results indicate that the capillary exhibits better collimation for heavy ions. In addition, the transmission of direct beams at different air pressures is observed. Heavy ions lose less energy at the same pressure; however, their trajectories are more divergent. The direct beam ions are not affected by the scattered ions at 100 Pa, making it feasible to perform MeV-SIMS analysis under ambient pressure.

Keywords MeV-SIMS · Glass capillary · Focusing effect · Monte Carlo simulation · Ion-capillary interactions · Air pressure

1 Introduction

Observing molecular distribution in biological tissue and cells helps elucidate life phenomena and develop new drugs [1]. Molecular imaging is important in biomedical research. For biological and polymer samples, understanding both elemental composition and molecular distribution characteristics is necessary. Secondary-ion mass spectrometry (SIMS) [2] is a highly surface-sensitive analytical method that reveals chemical composition of surface layers and characterizes molecular structure of organic materials [3]. However, conventional SIMS uses incident ions with energies from 0.5 to 30 keV [2] to sputter samples (namely, keV-SIMS), interacting through nuclear collisions, causing severe molecular fragmentation. When analyzing intact macromolecules (e.g., greater than 500 Da) in biomedical, pharmacy, and polymer chemistry research, low-energy incident ions cause severe fragmentation through nuclear collisions, making it difficult to sputter entire macromolecules from the surface [4, 5].

To address the issue of low yields of non-fragmented molecular ions obtained by conventional (keV) SIMS, a novel SIMS method using fast (MeV), heavy primary

This work was supported by the Fundamental Research Funds for the Central Universities (Nos. 20838044E0020 and 2022SCU12124), and the Natural Science Foundation of Sichuan Province (Nos. 2023NSFSC1317 and 2023NSFSC0051).

✉ Yi-Han Wang
yhwang027@scu.edu.cn

[1] Key Laboratory of Radiation Physics and Technology of the Ministry of Education, Institute of Nuclear Science and Technology, Sichuan University, Chengdu 610064, China

ions instead of keV primary ions, MeV-SIMS, has gained increasing scientific attention in recent years [6–9]. The basic principles of the two SIMS methods are almost identical; however, the secondary ions are generated via distinct mechanisms. In contrast to keV-SIMS, the desorption of secondary ions in MeV-SIMS is mainly caused by electronic excitation rather than nuclear collisions, which allows for softer desorption of molecules and thereby yields intact molecules by several orders of magnitude [7]. In recent years, MeV-SIMS has emerged as a powerful tool for analyzing and imaging molecular morphology, and has been widely used in various fields, including biomedicine [10], organic chemistry [11], forensic science [12] and cultural heritage [13]. These results demonstrate significant advantages and potential in analyzing large molecules.

The imaging method based on focused primary ion-beam scanning relates to focusing requirements of high-energy heavy ions. The imaging mode in biomedical research must form a microbeam with spot size in the low micron range for cellular-level resolution. Due to high magnetic stiffness of high-energy heavy ions, conventional quadrupole lens technique struggles to achieve focusing over short distances. Similar spot sizes can be achieved via a tapered glass capillary [14–16]. Its tapered geometry and micron-sized outlet achieve beam collimation and focusing to a few microns while providing clear sample viewing. The capillary can function as a vacuum isolator, allowing ions into gaseous environments without separating membranes [7]. Capillaries were thus used as microprobes for in-air particle-induced X-ray emission [17], nuclear reaction analysis [18], Rutherford backscattering spectrometry [19], scanning transmission ion microscopy [14], X-ray radiography [20], ion-beam writing [21] and cell irradiation [22]. Another function of the capillary is enhancing output beam current density. Research groups worldwide have investigated the enhancement mechanism by observing transmission of various charged particles in different capillaries, including highly charged ions [23–26], singly charged ions [27–29], electrons [30–33], negative ions [34–36], positrons [37], and muons [38], in insulated nano-capillaries and glass capillaries. The charged particles studied have energies from several keV to several hundred keV, with their transmission mechanism well understood. The enhancement of beam current density occurs due to guiding effects of the Coulomb field from charge deposition on the inner wall surface. Capillaries also focus X-rays through total internal reflection [39–41]. For MeV ions, Nebiki et al. [42] discovered that 2 MeV He beam density was greatly enhanced by a capillary in 2003. Hasegawa et al. [43] proposed the enhancement for MeV protons mainly results from small-angle scattering. Simon et al. [16] verified that the guiding effect becomes ineffective at higher ion energies through measurements of 1 MeV He ions and 71 MeV Xe ions, showing that enhancement occurs through elastic scattering. Liu et al. [44] demonstrate that for 1 MeV proton transmission, focusing occurs through atomic scatterings when tilt angle is below cone angle. While these studies attribute the enhancement to elastic scattering, a quantitative description of scattering effects on MeV heavy-ion transmission, multiple scattering events, and recoil process is lacking. Understanding these interactions aids in selecting appropriate ion beams and developing capillary microprobes for high-resolution SIMS imaging.

To clearly observe the change in the motion state of the incident ions after scattering and the physical behavior of the recoil atoms, a Monte Carlo simulation program based on the Stopping and Range of Ions in Matter (SRIM) software [45] was developed. In this paper, we describe the ability of a tapered glass capillary to collimate or focus MeV heavy-ion beams and analyze in detail the physical behaviors of MeV heavy ions after interacting with the capillary wall, as well as the effect of air pressure in the chamber on ions' flight. Section 2 describes the layout of the MeV-SIMS chamber. Section 3 briefly describes the parameters and methodology of the Monte Carlo. Section 4 analyzes the scattering and recoil behavior of 6 MeV Si, Ar, and I ion beams after colliding with the capillary wall, which provides a clear description of the motion state of the scattered ions and recoil atoms. Their spatial distributions in the target area were observed, demonstrating that the core of the primary ion beam was well separated from the surrounding scattered ions and recoil atoms. Multiple scattering events occurring in the capillary were calculated to understand the effect of the number of scattering events on the spatial distribution. In addition, the effect of the air pressure in the chamber on the direct beams was studied. Finally, the conclusions are presented in Sect. 5.

2 MeV-SIMS units under construction

MeV-SIMS has been developed in the world's top ion-beam laboratories in recent years [6–9]. A microbeam megaelectron volt time-of-flight secondary-ion imaging mass spectrometer (MeV-TOF-SIMS imaging) based on a 3 MV tandem accelerator is planned at Sichuan University [46], depicted in Fig. 1(a), as China's first MeV-TOF-SIMS imaging. A capillary microprobe system will be used, as shown in Fig. 1(b). The MeV ion beam enters the chamber via slits that reduce the beam spot size to the inlet diameter of the capillary. The insulated glass capillary is mounted in a grounded metal tube to shield it from electrostatic stray fields from capillary charging [7]. After entering, some ions pass through directly, while others exit after one or several scatterings with the capillary wall at angles larger than the taper angle, as shown in Fig. 1(c). This figure shows the scattering in the narrowed

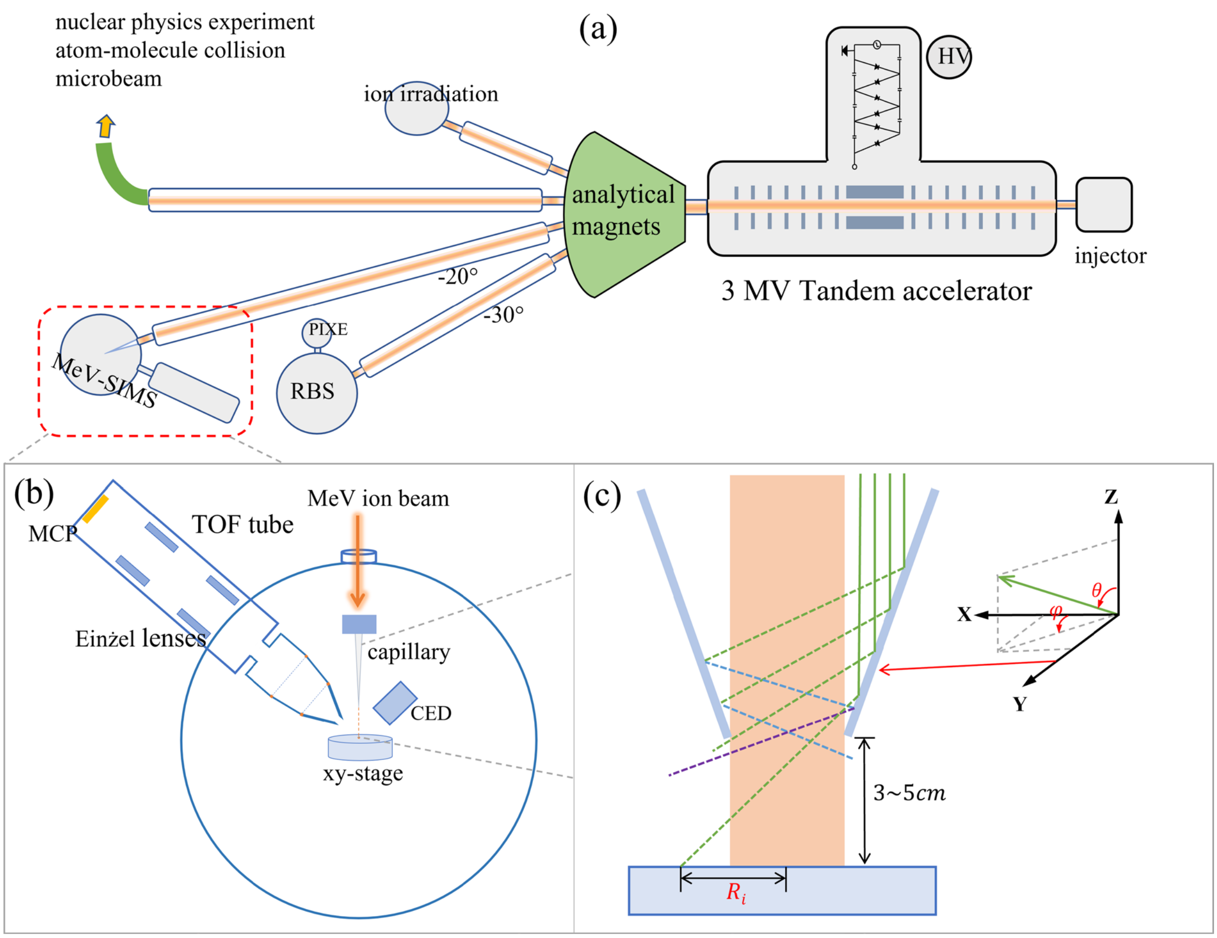

Fig. 1 (Color online) (**a**) Schematic layout of the MeV-SIMS device based on a 3 MV tandem accelerator; (**b**) schematic of the chamber for capillary-based MeV-SIMS; (**c**) ion trajectories in the capillary, where some ions can exit the capillary directly without colliding (orange) and others exit it via one scattering (green), second scattering (blue), or multiple scatterings (purple)

part, excluding the straight part where ion scattering is unlikely. The spherical coordinate system in Fig. 1(c) is established with the collision point as origin, capillary bus as *Y* axis, and normal of capillary wall as *Z* axis. The polar angle θ indicates the angle between outgoing direction and *Z*-axis, while azimuth angle φ indicates the angle between the projection of outgoing direction on the wall surface and *X*-axis, determining the deviation degree.

The distance between the capillary tip and the sample platform is 4 cm; thus, all the ions exiting the capillary undergo a flight path with a horizontal displacement of 4 cm to reach the target. During the measurements, the secondary ions were sputtered and extracted into a linear time-of-flight (TOF) tube. They are then constrained by two sets of Einzel lenses before reaching the microchannel plate detector (MCP) at the end of the TOF tube, which generates a stop signal. Secondary electrons generated when the primary ions strike the sample surface are collected by a Channeltron electron detector (CED) [47] to trigger the start signal. Therefore, the mass-to-charge ratio of the secondary ions can be deduced from the time difference between the start and stop signals.

3 Monte Carlo simulation method

Capillaries are typically made of borosilicate glass, which is easier to process for mass production than soda-lime or quartz glass because of its low cost and ability to soften significantly at approximately 800 °C [48]. In general, the inner diameter of the capillary inlet was approximately 1 mm, and its outer diameter did not exceed 2 mm. The outlet diameter, that is, the inner diameter of the capillary outlet (tip), ranged from 1~10 μm, depending on the object under analysis. The capillary has a taper angle ranging from 0.1° to 1°.

To enhance the observation of the ion-capillary interaction process, we identified the maximum critical parameters of the capillary in the simulation: an inlet diameter of 2 mm, outlet diameter of 10 μm, taper angle of 1°, and wall thickness of 150 μm, which is the thickness of a typical borosilicate glass tube [48]. Therefore, we conducted simulations on this capillary. At the beginning of the simulation, using the TRIM part in SRIM, Si, Ar, and I primary ions with energies of 6 MeV were sequentially selected to observe the difference between the different masses of heavy ions after interacting with the capillary and their spatial distributions on the sample surface. These ions were incident parallel to the capillary axis; therefore, their incident angle on the capillary wall was set to 89°, which is equal to the taper angle, with a total of 10^4 random ions. Then, borosilicate glass in the compound dictionary was selected as the target layer, and its thickness was set. The atomic percentages in this borosilicate glass were 61% O, 26% Si, 9% B, 3% Na, and 1% Al. The displacement energy of each element, which can affect the sputtering yield, must be changed according to Ref. [49].

The numerical calculation program used in the simulation is Python. For convenience, a tapered glass capillary can be viewed as a perfect cone, ignoring the roughness of its inner surface and nonuniformity of its wall thickness. The ion beam entering the capillary was simulated to be perfectly collimated with no divergence. Scattering and sputtering information for each ion beam after collision with the capillary were obtained by SRIM and saved in the so-called "BACKSCAT" and "SPUTTER" files, respectively, which tabulates the kinetics of ions or atoms leaving the target. The energies and outgoing directions (cosines of the final trajectory) of the scattered ions and recoil atoms in these files were then used in Python, where the geometric conditions of the capillary and position of the sample stage were set. While the exit positions of the scattered ions or recoil atoms differ from their collision positions, their average separation remains within a few nanometers. Consequently, they can be treated effectively by exiting from a common point (the collision point) in our simulation.

SRIM software is specifically designed for ion-matter interactions, making it highly accurate for simulating ion implantation, sputtering, and radiation damage. It has been widely used to simulate the physical properties of energetic ions after their interaction with materials. It not only has built-in models for simple elastic collisions and more complex cascade collisions but also considers the electronic energy loss during continuous scattering and sputtering events. The details of each ion-atom collision in the cascade collisions are recorded. Any combination of ions and target materials can be easily selected on an intuitive user interface, unlike other Monte Carlo software such as Geant4 and MCNP. Therefore, it can be used to directly and reliably simulate the transmission of ions through glass or other capillaries. Some of the above features are not always available in other simulation methods. For example, Geant4 cannot provide information about atoms sputtered from surfaces.

4 Results and discussion

As shown in Fig. 1(c), the ions leaving the capillary can be divided into two categories: ions that exit directly without contacting the capillary (called the direct beam) and ions that exit after scattering with the capillary (called the scattered ions). The collision of the primary ion beam with the capillary wall is accompanied by a recoil process in addition to the scattering process. In this section, the main physical processes of heavy ions interacting with the capillary are discussed, including first scattering (Sect. 4.1), multiple scatterings (Sect. 4.2), and recoil processes (Sect. 4.4). This section mainly focuses on the observation of the energy and spatial distributions of heavy ions in the target area after undergoing these physical processes. In addition, the effect of air pressure on the transmission of the direct beam is considered in Sect. 4.4. Therefore, we describe the following aspects:

4.1 First scattering

When primary ions enter the capillary, ions can collide with the capillary wall resulting in different outcomes: i) ions lose energy after collisions inside the wall and become interstitial atoms, ii) ions undergo low-angle Rutherford scattering and scatter forward, iii) ions undergo Rutherford backscattering (few), and iv) ions can penetrate the wall at the capillary tip. Because the ion range within the wall is smaller than its thickness, iv) is not possible. Forward-scattered ions can exit the capillary after first scattering, while others collide with the opposite wall and experience similar outcomes depending on scattering angles. This subsection discusses energy and angular distributions of incident ions after first scattering, and energy and spatial distributions of scattered ions leaving the capillary in the target area. An area with a diameter of 1 cm was selected as the target area in the simulation.

Figure 2(a)–(c) shows the energy distributions of 6 MeV Si, Ar, and I ions after their first scattering in the capillary. The energy of Si ions is mainly distributed in 0~3 MeV, with an average of 2.1 MeV; that of Ar ions falls mainly within 0~4 MeV, averaging to 2.7 MeV; that of I ions is mainly within 4~6 MeV, showing an average of 4.3 MeV. The greater the ion mass, the less energy lost after scattering; thus, the process affects lighter ions more at the same energy. This result suggests that using heavier ions for experimental analysis to obtain more focused energy beams with capillary collimation is feasible. The energy loss occurs from scattering of surface and internal atoms within 100 nm from the surface, accompanied by motion direction changes. Scattered ions show azimuth

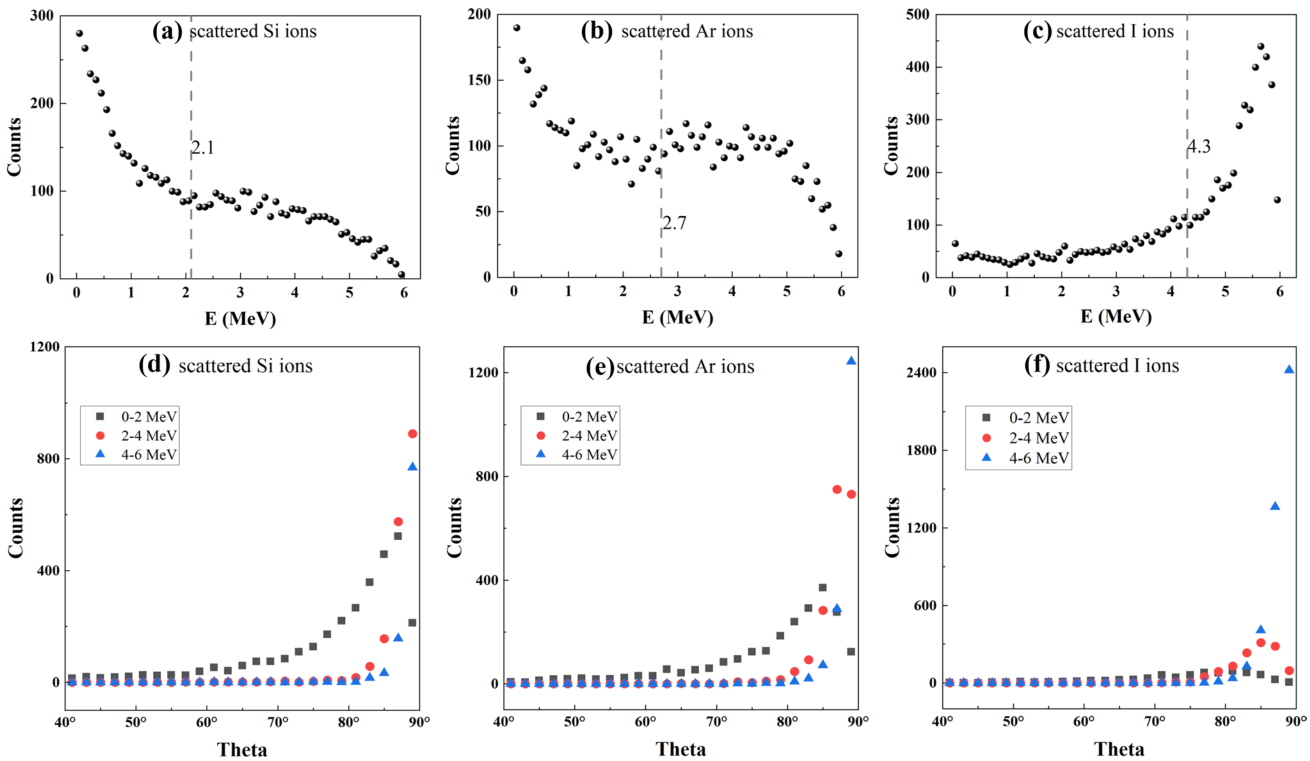

Fig. 2 (Color online) (a)–(c) Energy distributions of three primary ions after their first scattering at a collision point in the capillary, with dashed lines indicating their average energies; (d)–(f) their polar angle distributions in different energy intervals

angle symmetry but distinct polar angle distributions. Figure 2(d)–(f) shows scattered ions counted in three energy intervals. Low-energy ions have wider angular distribution (70°~90°) with fewer counts, while middle and high-energy ions concentrate in 80°~90° range. Higher energy scattered ions have greater polar angles, making them more likely to exit the capillary. Heavier ions have smaller polar and azimuth angle distributions. According to the Rutherford scattering phenomenon, when the incident ion mass differs greatly from that of the stationary target atom, less energy is transferred to the target atom, resulting in less energy loss.

Not all scattered ions can exit the capillary—only ions with small scattering angles that exceed the cone angle are ejected from the capillary and reach the target surface through vacuum flight. The two-dimensional spatial distributions of three scattered ions in the target area are observed as scattered ions' halos, shown in Fig. 3(a)–(c). We observe minimal ions within a 0.8 mm radius, aligning with the experimental and simulated distribution of the capillary-collimated 5 MeV Si primary beam at the target in Ref. [8]. In that study, using a smaller capillary geometry, no scattered ions were detected within 0.5 mm. These ion halos are concentrated within a radius of 1~3 mm from the target center, suggesting that even if the ions exiting the capillary have an extremely small exit angle, they can still reach positions far from the target center owing to their vacuum flight distance exceeding the capillary outlet diameter. The direct beam, with a 5 μm radius, remains well separated from surrounding scattered ions whose energies are attenuated after scattering. This result demonstrates the capillary's potential for fixed-point sample measurement and indicates optimal sample stage movement during focused primary ion-beam scanning.

As mentioned earlier, the energy of scattered ions relates to their exit angle, requiring observation of their spatial distribution and landing position. Figure 3(d)–(f) shows radius distributions of scattered ions in the target region at three energy intervals, counted from the center of halos along the positive x-axis. Ion distributions vary across energy intervals, with high-energy ions (4~6 MeV) showing smaller distribution ranges near the target center. Si ions predominantly range from 2~6 MeV, Ar ions from 3~5.5 MeV, and I ions from 5~6 MeV. Heavier ions show greater proportion in the high-energy part. These factors indicate that heavier ions (such as I ions)experience less energy loss after scattering, have a lower likelihood of becoming interstitial atoms within the capillary wall, and show higher scattering rates. Thus, the capillary provides better collimation for heavier ions.

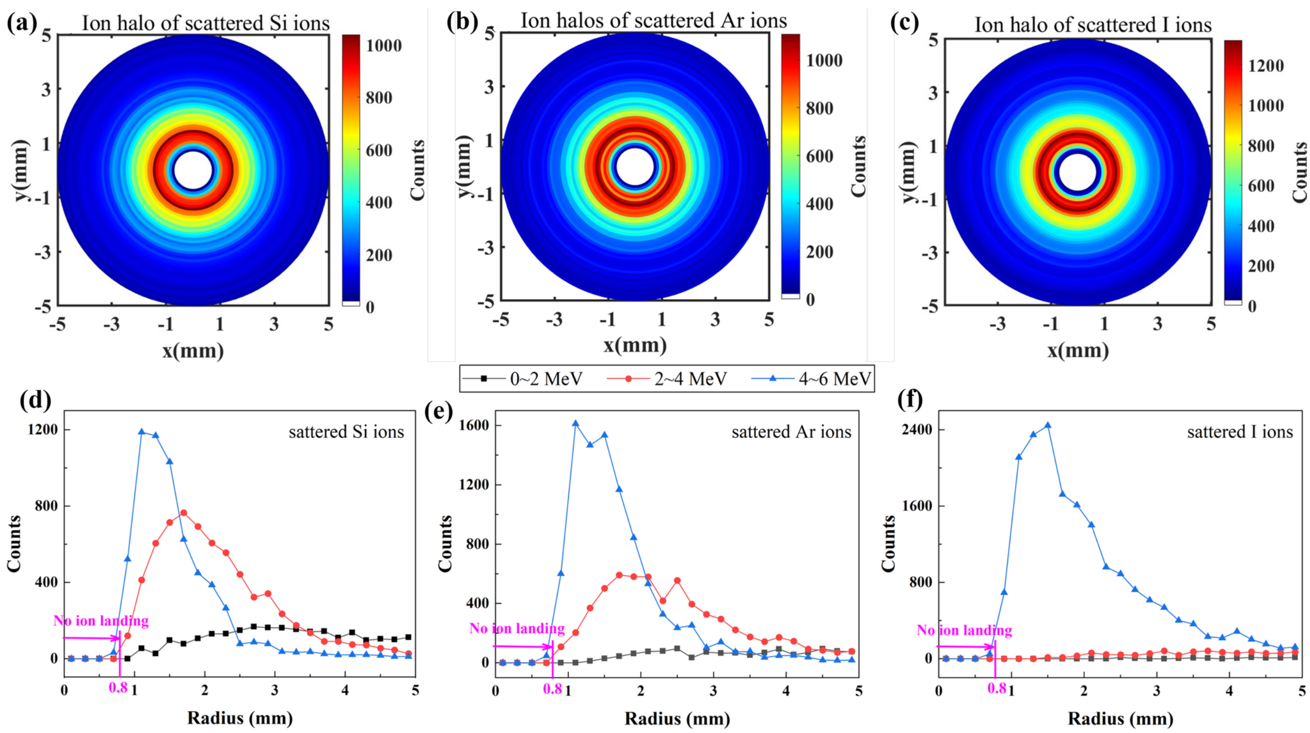

Fig. 3 (Color online) (a)–(c) Two-dimensional spatial distributions of three scattering ions in the target area after exiting the capillary; (d)–(f) their radius distributions in different energy intervals

4.2 Ion halos from multiple scatterings

As some ions have large scattering angles, they may continue to collide with the capillary, leading to multiple scatterings. This subsection calculates the maximum number of ion scatterings and observes the ion halo after each scatter. Some incident ions may scatter multiple times in the capillary, with increasing scattering angles and decreasing vertical distance between collision points until reaching the outlet. The number and energy of outgoing ions decrease after each scattering, landing farther from the target center. Therefore, we focus on the ions reaching the target area after each scattering. Ion information for up to three scatterings needs calculation, based on simulation parameters including capillary geometry, working distance, and target area size. Figure 4 shows the ion halos from each scattering. The ions in the target area decrease significantly after second scattering, mainly distributing outside 1 mm from target center. After the third scattering, extremely few ions reach the target area and are more than 3 mm away. The halo patterns after three scatterings are shown in the last column in Fig. 4, similar to ion halos from first scattering in Fig. 3(a)–(c). They distribute beyond 0.8 mm from target center, mainly within 1–3 mm. Figure 5 shows energy distributions of halo ions after each scattering. The energy spectrum after first scattering and total scatterings are nearly identical, especially within 3~6 MeV. Low-energy differences result from other scatterings. The number and energy of outgoing ions decrease after each scattering, with less than 0.2% probability for the ions to reach the target after multiple scatterings. The outgoing angle increases per scattering, causing ions to land farther from center. Thus, first scattering dominates among multiple scattering events.

4.3 Recoil atoms from the first collision

When the primary ion beam incidents the capillary wall at a low angle, recoil and scattering processes occur. During elastic collision between incident ions and wall atoms, ions are scattered and lose energy to the wall atoms. If displaced wall atoms reach the surface with kinetic energy exceeding surface binding energy, they emerge from the surface—a process called recoil. These recoil atoms may contaminate the sample surface or cause sputtering when highly energetic. This section examines the energy and spatial distributions of recoil atoms in a finite target region to understand their impact on sample analysis.

Similar to the scattered ions, the recoil atoms show a distribution pattern at polar angles. Figure 6 shows the count of recoil atoms per degree at a collision point, concentrated within $0^\circ \sim 60^\circ$ at the polar angle, corresponding to $30^\circ \sim 90^\circ$ to the capillary wall. The phenomenon shows that the solid

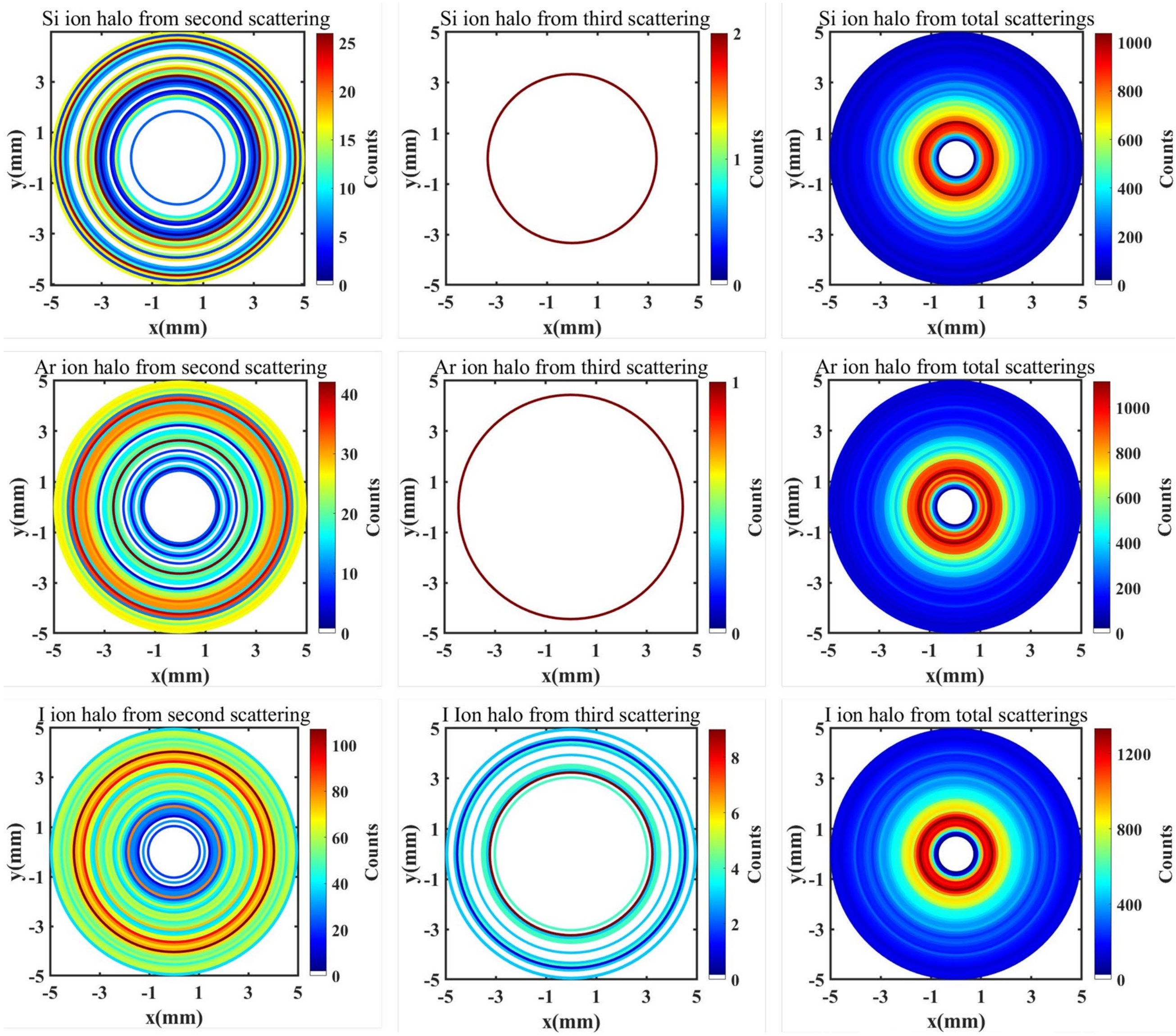

Fig. 4 (Color online) Ion halos from each scattering

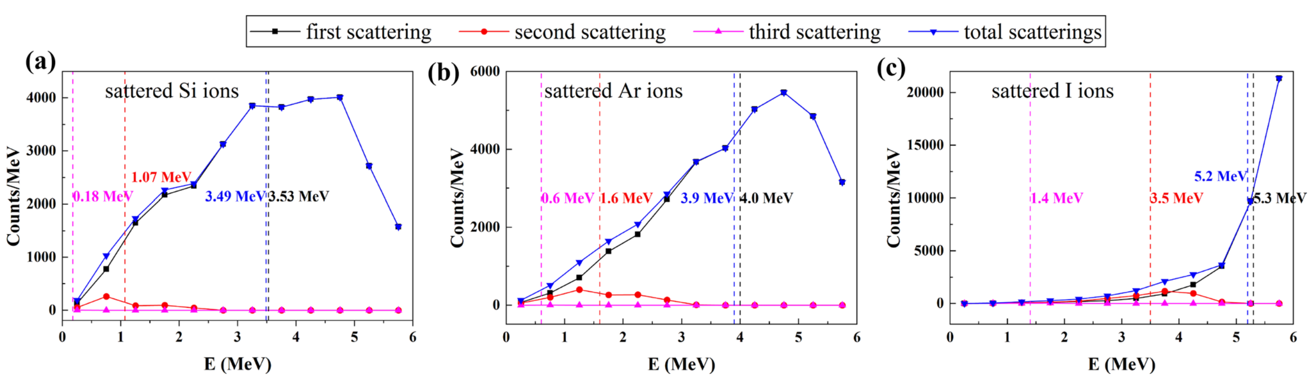

Fig. 5 (Color online) Energy distributions of scattered ions coming out of the capillary and landing in the target area after the first (black line), second (red line), third (green line) and total scattering (blue line), respectively. Dashed lines of the same color indicate the average energy of those scattered ions

angle of recoil atoms in the outgoing direction exceeds that of scattered ions, making it harder for them to exit the capillary. The counts reflect the recoil yield of wall atoms, related to their proportion in the capillary and atomic characteristics (e.g., mass, displacement energy).

Figure 7 shows the energy distributions of wall atoms recoiled by Si, Ar, and I ion beam in the target region. The recoil yield of high-energy heavy ions on wall atoms is high (20~180 atoms per ion), but few wall atoms can exit the capillary and reach the target area, with most having energies below 0.4 keV (about 90%). This confirms that recoil atoms struggle to exit the capillary due to large recoil angles, as atoms with small outgoing angles may exit and reach the target area. Figure 8 shows the radius distributions of recoil atoms' drop points in the target area,

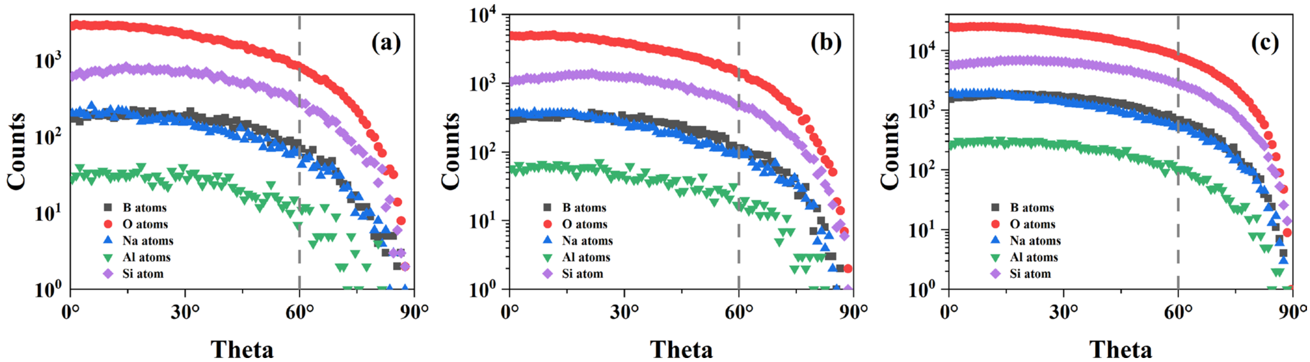

Fig. 6 (Color online) Distributions of these recoil atoms over the polar angle at a collision point in the capillary: (**a**) Recoiled by Si-ion beam, (**b**) recoiled by Ar-ion beam, and (**c**) recoiled by I-ion beam

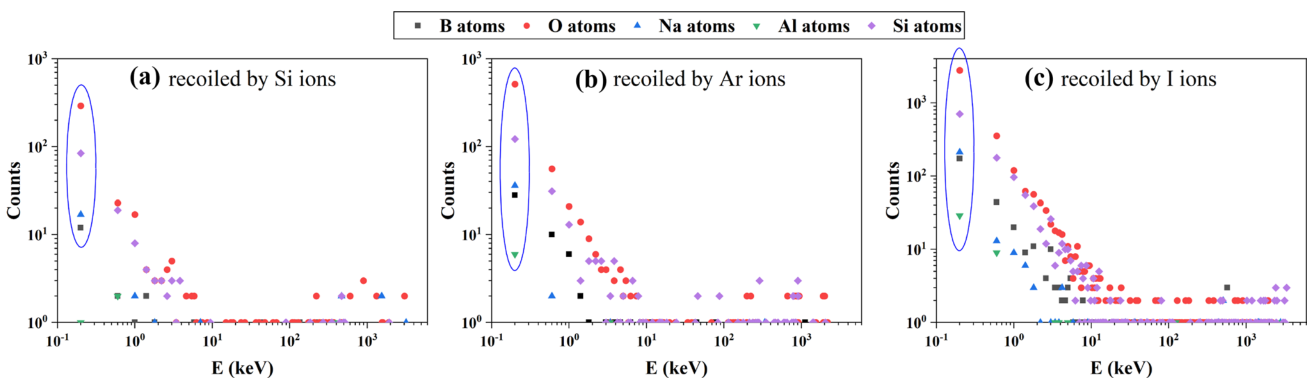

Fig. 7 (Color online) Energy distributions of recoil atoms in the target area, after exiting the capillary

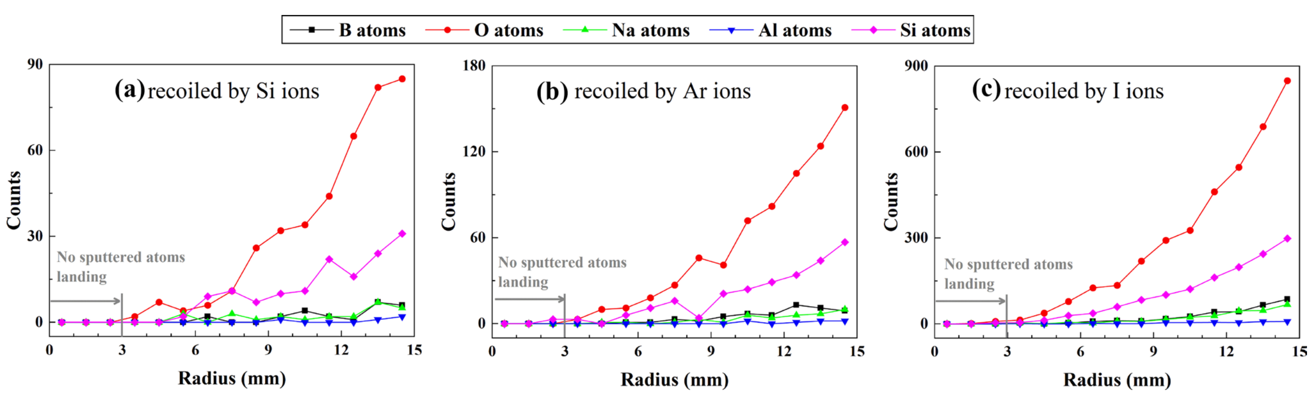

Fig. 8 (Color online) Radius distribution of recoil atoms reaching the target area

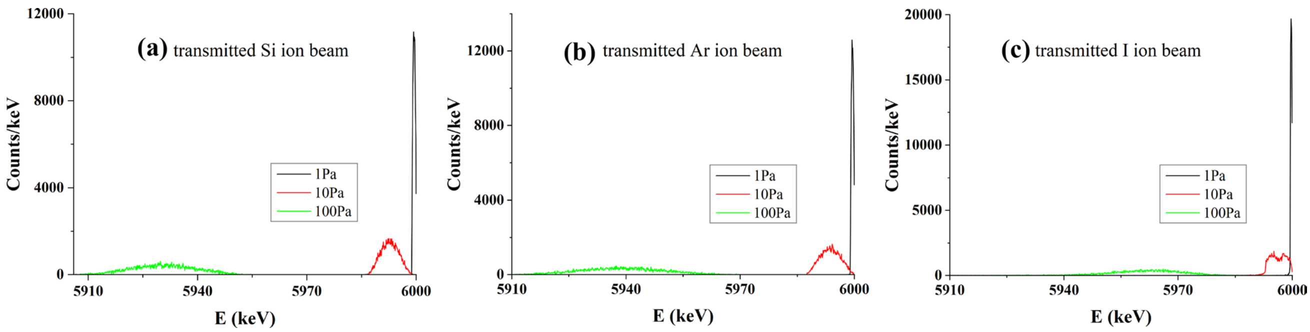

Fig. 9 (Color online) Effect of air pressure in the chamber on direct beam energy: (**a**) Transmitted Si ions, (**b**) transmitted Ar ions, and (**c**) transmitted I ions

displaying a distribution beyond 2 mm from the center, without affecting the direct beam area with 5 μm radius.

Because of the large exit angles and low energy of the recoil atoms, most atoms can collide with the wall multiple times, resulting in multiple recoil events. The number of recoil atoms and their energy decrease after each collision. Thus, only a small number of recoil atoms with low energies can exit the capillaries and reach the sample surface; therefore, they do not constitute a new source of contamination or sputtering to the sample in the subsequent analyses.

4.4 Effect of air pressure on the transmission of direct beams

The scattered ions and recoil atoms move in an ideal vacuum condition. If the chamber is in a medium or low vacuum, it affects both the trajectory of scattered ions/recoil atoms and the stable transmission of the direct beam. Since the halos of scattered ions and recoil atoms are distant from the direct beam, their trajectories and energies diverge further in air, exceeding the TOF tube range. This subsection focuses on the air environment's effect on the direct beam.

The inside of the capillary has high vacuum, while medium or low vacuum exists outside it; thus, the direct beam must penetrate a 4 cm gas target to reach the sample. Figure 9 shows the energy distributions of 6 MeV Si, Ar, and I ion beams at different air pressures. Higher pressure causes greater attenuation and energy broadening, whereas pressures below 1 Pa barely affect the ion energy. The energy of heavier ions is less affected by air pressure, shown by the rightward peak shift, owing to the less energy loss at 6 MeV incident energy (Fig. 10). This energy loss pattern remains consistent at other pressures.

In addition to the attenuation and broadening of ion energy, its trajectory is affected. Figure 11 shows radius distributions of drop points of direct beams on the target after passing through gases at different pressures, with shaded areas showing radius broadening. Higher air pressure causes greater deviation from the original trajectory and wider radius spread, due to denser gas molecules increasing collision likelihood between incident ions and air atoms. Heavier incident ions show more trajectory divergence than lighter ions (I>Ar>Si) under the same pressure, as ions with large masses and radii have larger collision cross sections. I ions are the most diffused at a 100 Pa pressure with drop-point radii widening to 360 μm; however, they do not touch the scattered ion halos, suggesting that the MeV-SIMS chamber can operate under medium- or low-vacuum conditions. While heavier ions show smaller energy loss and broadening through the gas target, their more divergent trajectories disadvantage SIMS imaging. Therefore, balancing ion mass and energy is crucial for subsequent SIMS analysis.

5 Conclusion

A Monte Carlo simulation program using SRIM software was developed to observe scattering and recoil behaviors of high-energy heavy-ion-beam interactions with a conical glass capillary. Changes in the incident ions' motion state after first scattering with the capillary wall were analyzed. Heavier ions showed smaller scattering angles and less energy loss after scattering and were thus more likely to exit the capillary and reach the target area, indicating better capillary collimation for heavier primary ions. The spatial distributions of scattered ions in the target area fell outside a 0.8 mm radius from the target center, allowing separation of

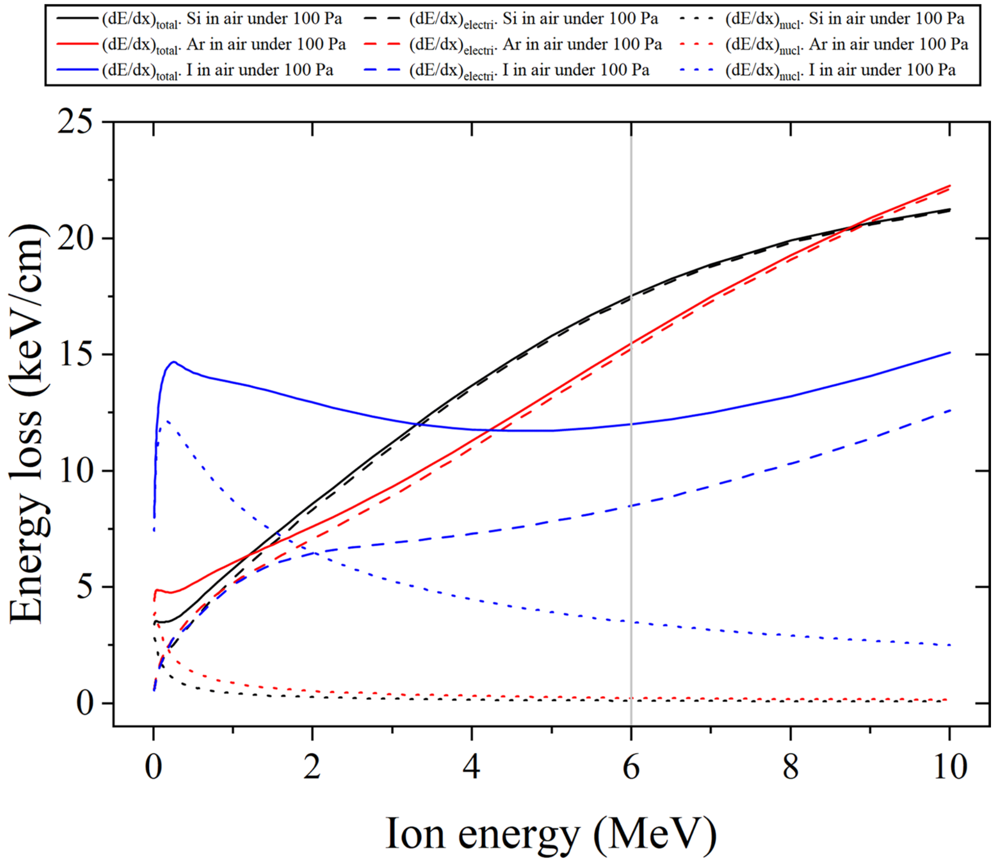

Fig. 10 (Color online) Energy loss of direct beams in air under 100 Pa, obtained from SRIM calculations for demonstrating the energy loss regimes. The dashed, dotted, and solid lines show the electronic, nuclear, and total energy losses, respectively

direct beam from scattered ions. Although three scattering events were calculated in simulations, only the first scattering event needs consideration in actual experiments due to its dominance among multiple scatterings. Most recoil atoms have sub-keV energies (< 0.4 keV), and few reach the target area through the capillary, falling 2 mm from the target center. These findings show that the recoil atoms neither affect the direct beam analysis nor cause sample contamination and sputtering, meeting our requirements. Additionally, the air pressure effects on the direct beam flight are considered. Higher air pressure increases the direct-beam-energy attenuation, which can be reduced by heavier ion beams; however, heavier atoms experience more dispersed trajectories. I ions show the maximum divergence at 100 Pa with their drop-point radius reaching 360 μm; however, they still do not overlap the position of the scattered ions.

Although heavier ions have less energy loss after scattering, their trajectories are more affected by gas in non-high vacuum. The relationship between ion mass and energy must be balanced when choosing an incident ion beam. The energy loss regime of primary ions can be calculated by SRIM to select appropriate ion type and energy. Higher ion energy and greater ion mass are more suitable for analyzing macromolecular samples. In our simulations, helium proved the most promising protective gas to replace air, as it greatly mitigates heavy-ion flight path dispersion. The findings verify that the capillary has good focusing ability for MeV heavy ions and potential for MeV-SIMS under ambient pressure. This study provides a solution for laboratories without magnetic or electrostatic lenses and builds the foundation for MeV-SIMS chamber development.

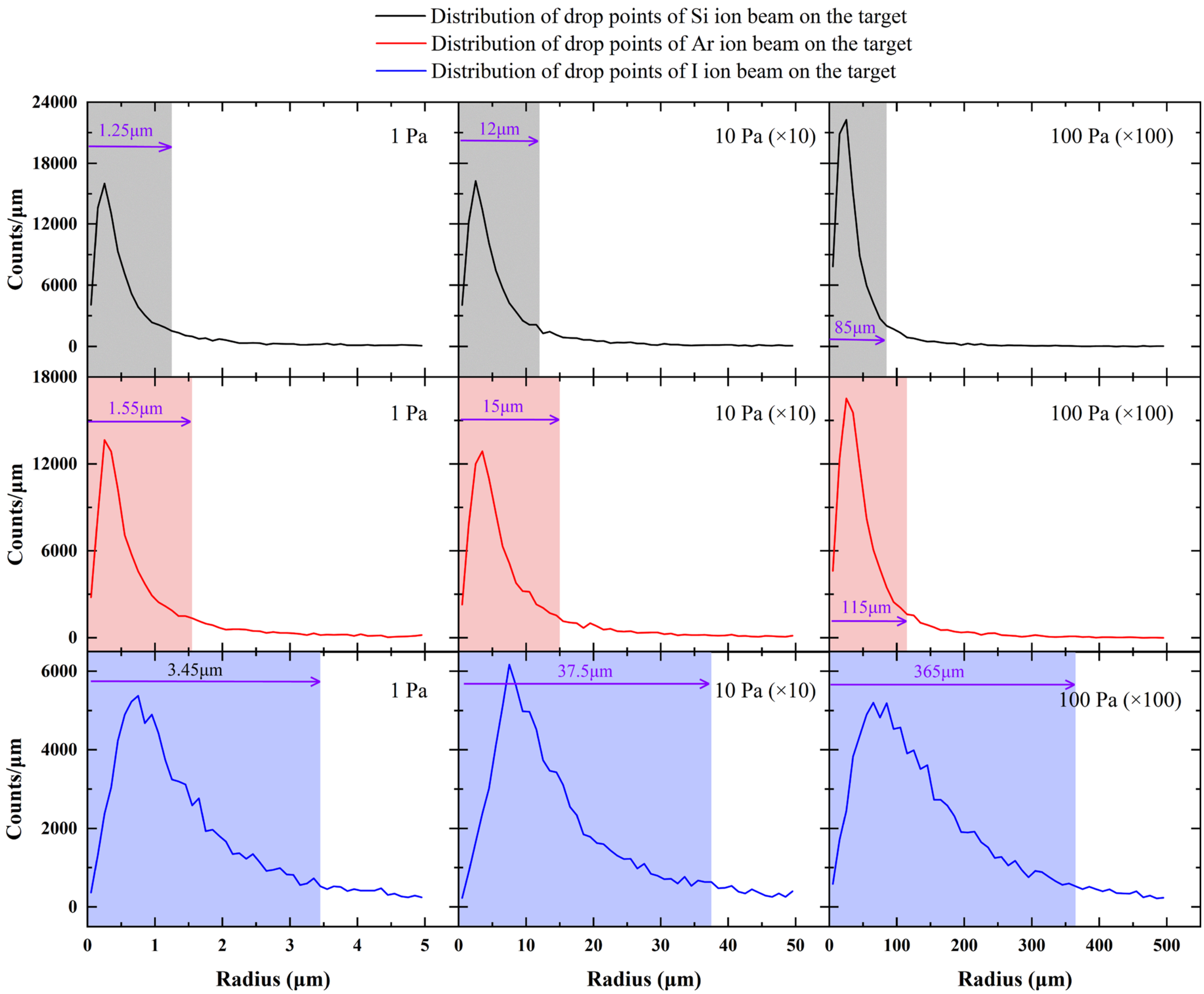

Fig. 11 (Color online) Effect of air pressure in the chamber on the direct beam's trajectory. The width of the shaded area in the figure indicates the spread of the radius of the drop points. The numbers in parentheses indicate that the original count (in vertical coordinate) at this pressure has been expanded by a factor of 10 or 100, to standardize the counts at different pressures

Acknowledgements We would like to thank our colleague at Sichuan University, Researcher Zhu An, for his suggestions on this work.

Author Contributions All authors contributed to the study conception and design. Simulations were performed by Ji-Wei Lai. Data collection and analysis were performed by Tong-Tong Zhu and Ming-Ming Yu. Formal analysis and investigation were conducted by Yun-Peng Cao and Hong-Wen Cao. This work was supported by Yi-Han Wang and Kun Zhang. The first draft of the manuscript was written by Ji-Wei Lai, and all authors commented on previous versions of the manuscript. All authors read and approved the final manuscript.

Data availability The data that support the findings of this study are openly available in Science Data Bank at https://cstr.cn/31253.11.sciencedb.j00186.00902 and https://www.doi.org/10.57760/sciencedb.j00186.00902.

Declarations

Conflict of interest The authors declare that they have no conflict of interest.

References

1. D.F. Cobice, R.J.A. Goodwin, P.E. Andren et al., Future technology insight: mass spectrometry imaging as a tool in drug research and development. Br. J. Pharmacol. **172**, 3266–3283 (2015). https://doi.org/10.1111/bph.13135
2. J.C. Vickerman, in *Surface analysis—the principal techniques*, 2nd edn., ed. by J.C. Vickerman, I.S. Gilmore (Wiley, Chichester, 2009), p. 113 https://doi.org/10.1002/9780470721582.ch4
3. Z.P. Li, Time-of-flight secondary ion mass spectrometry. Bull. Mineral. Petrol. Geochem. **39**, 1173–1190 (2020). https://doi.org/10.19658/j.issn.1007-2802.2020.39.104. (**in Chinese**)
4. L.S. Cai, M.C. Xia, Z.P. Li et al., Bioimaging by secondary ion mass spectrometry. Prog. Chem. **33**, 97–110 (2021). https://doi.org/10.7536/PC200458. (**in Chinese**)
5. L.M. Sun, Applications of time-of-flight secondary ion mass spectrometry in biomaterials and life science (Part II). J. Chin. Mass Spectrom. **35**, 385–396 (2014). (**in Chinese**)
6. L. Jeromel, Z. Siketić, N. Ogrinc Potočnik et al., Development of mass spectrometry by high energy focused heavy ion beam: MeV SIMS with 8 MeV Cl^{7+} beam. Nucl. Instrum. Methods Phys. Res. Sect. B **332**, 22–27 (2014). https://doi.org/10.1016/j.nimb.2014.02.022
7. KU. Miltenberger, M. Schulte-Borchers, M. Döbeli et al., MeV-SIMS capillary microprobe for molecular imaging. Nucl. Instrum. Methods Phys. Res. Sect. B **412**, 185–189 (2017)
8. M. Brajković, M. Barac, D. Cosic et al., Development of MeV TOF-SIMS capillary microprobe at the Ruđer Bošković Institute in Zagreb. Nucl. Instrum. Methods Phys. Res. Sect. B **461**, 237–242 (2019). https://doi.org/10.1016/j.nimb.2019.10.006
9. T. Seki, K. Ishii, T. Aoki et al., Secondary ion mass spectrometry measurements under ambient and humid conditions using MeV ions. J. Vac. Sci. Technol., B **38**, 034014 (2020). https://doi.org/10.1116/1.5145014
10. M. Popović Hadžija, Z. Siketić, M. Hadžija et al., Study of the diacylglycerol composition in the liver and serum of mice with prediabetes and diabetes using MeV TOF-SIMS. Diabetes Res. Clin. Pract. **159**, 107986 (2020). https://doi.org/10.1016/j.diabres.2019.107986
11. M. Barac, M. Brajković, I. Bogdanović Radović et al., MeV TOF SIMS analysis of hybrid organic/inorganic compounds in the low energy region. J. Am. Soc. Mass Spectrom. **32**, 825–831 (2021). https://doi.org/10.1021/jasms.1c00006
12. M. Barac, A. Filko, Z. Siketić et al., Comparison of optical techniques and MeV SIMS in determining deposition order between optically distinguishable and indistinguishable inks from different writing tools. Forensic Sci. Int. **331**, 111136 (2022). https://doi.org/10.1016/j.forsciint.2021.111136
13. M. Krmpotić, D. Jembrih-Simbürger, Z. Siketić et al., Study of UV ageing effects in modern artists' paints with MeV-SIMS. Polym. Degrad. Stab. **195**, 109769 (2022). https://doi.org/10.1016/j.polymdegradstab.2021.109769
14. M.J. Simon, M. Döbeli, A.M. Müller et al., In-air STIM with a capillary microprobe. Nucl. Instrum. Methods Phys. Res. Sect. B **273**, 237–240 (2012). https://doi.org/10.1016/j.nimb.2011.07.084
15. Z.Y. Gong, S. Yan, H.J. Ma et al., Study of tapered glass capillary focusing MeV ion beam. Nucl. Instrum. Methods Phys. Res. Sect. B **272**, 370–373 (2012). https://doi.org/10.1016/j.nimb.2011.01.103
16. M.J. Simon, C.L. Zhou, M. Döbeli et al., Measurements and 3D Monte Carlo simulation of MeV ion transmission through conical glass capillaries. Nucl. Instrum. Methods Phys. Res. Sect. B **330**, 11–17 (2014). https://doi.org/10.1016/j.nimb.2014.03.016
17. T. Nebiki, M.H. Kabir, T. Narusawa, In-air PIXE analysis by means of glass capillary optics. Nucl. Instrum. Methods Phys. Res. Sect. B **249**, 226–229 (2006). https://doi.org/10.1016/j.nimb.2006.04.003
18. D. Sekiba, H. Yonemura, T. Nebiki et al., Development of microbeam NRA for 3D-mapping of hydrogen distribution in solids: application of tapered glass capillary to 6 MeV ^{15}N ion. Nucl. Instrum. Methods Phys. Res. Sect. B **266**, 4027–4036 (2008). https://doi.org/10.1016/j.nimb.2008.06.032
19. N. Fujita, K. Ishii, H. Ogawa, Development of In-Air-RBS method with tapered glass capillary. J. Phys: Conf. Ser. **194**, 142004 (2009). https://doi.org/10.1088/1742-6596/194/14/142004
20. J. Hasegawa, S. Shiba, H. Fukuda et al., A compact micro-beam system using a tapered glass capillary for proton-induced X-ray radiography. Nucl. Instrum. Methods Phys. Res. Sect. B **266**, 2125–2129 (2008). https://doi.org/10.1016/j.nimb.2008.02.051
21. T. Nebiki, T. Narusawa, (2006) Glass capillary optics for focusing of high energy ion beams, in. Int. Symposium Discharges Electr. Insulation Vacuum. **2**, 813–816 (2006). https://doi.org/10.1109/DEIV.2006.357427
22. Y. Iwai, T. Ikeda, T. Kojima et al., Ion irradiation in liquid of m^3 region for cell surgery. Appl. Phys. Lett. **2**, 23509–23511 (2008). https://doi.org/10.1063/1.2834695
23. H.Q. Zhang, N. Akram, C. Trautmann et al., Transmission profiles of ions through nano-capillaries of rectangular cross-section in mica. Nucl. Instrum. Methods Phys. Res. Sect. B **406**, 421–424 (2017). https://doi.org/10.1016/j.nimb.2017.01.039
24. H.Q. Zhang, N. Akram, R. Schuch, Transmission of highly charged ions through mica nanocapillaries of rectangular cross-section. Nucl. Instrum. Methods Phys. Res. Sect. B **408**, 61–66 (2017). https://doi.org/10.1016/j.nimb.2017.03.126
25. H.Q. Zhang, N. Akram, R. Schuch, Guiding and scattering of ions in transmission through mica nanocapillaries. Phys. Rev. A **94**, 032704 (2016). https://doi.org/10.1103/PhysRevA.94.032704
26. S.D. Liu, Y.T. Zhao, Y.Y. Wang, Simulations of guiding of low-energy ions through a single nanocapillary in insulating materials. Chin. Phys. B **26**, 106104 (2017). https://doi.org/10.1088/1674-1056/26/10/106104
27. A.X. Yang, C.Y. Zhu, Z. Qu et al., Taper angle dependence of the dynamical transmission of several-hundred-keV protons through PC conical capillary. Eur. Phys. J. D **74**, 192 (2020). https://doi.org/10.1140/epjd/e2020-10027-6

28. A.X. Yang, B.H. Zhu, S.T. Niu et al., Simulation of the dynamical transmission of several-hundred-keV protons through a conical capillary. Phys. Rev. A **97**, 052706 (2018). https://doi.org/10.1103/PhysRevA.97.052706
29. Y.F. Chen, X.M. Chen, F.J. Lou et al., Guiding of 60 keV O^+ ions through Al_2O_3 nanocapillaries with two different diameters. Acta Phys. Sin. **59**, 222–226 (2010). https://doi.org/10.7498/aps.59.222. (**in Chinese**)
30. P.F. Li, H. Yuan, Z.D. Cheng et al., Stable transmission of low energy electrons in glass tube with outer surface grounded conductively shielding. Acta Phys. Sin. **71**, 074101 (2022). https://doi.org/10.7498/aps.71.20212036. (**in Chinese**)
31. P.F. Li, H. Yuan, Z.D. Cheng et al., Dynamics of low energy electrons transmitting through straight glass capillary: Tilt angle dependence. Acta Phys. Sin. **71**, 084104 (2022). https://doi.org/10.7498/aps.71.20212335. (**in Chinese**)
32. L.B. Qian, P.F. Li, B. Jin et al., Transmission of electrons through the conical glass capillary with the grounded conducting outer surface. Acta Phys. Sin. **66**, 124101 (2017). https://doi.org/10.7498/aps.66.124101. (**in Chinese**)
33. C.L. Wan, P.F. Li, L.B. Qian et al., Dynamics of slow electrons transmitting through straight glass capillary and tapered glass capillary. Acta Phys. Sin. **65**, 204103 (2016). https://doi.org/10.7498/aps.65.204103. (**in Chinese**)
34. Q. Zhang, Z.L. Liu, P.F. Li et al., Transmission of low-energy negative ions through insulating nanocapillaries. Phys. Rev. A **97**, 042704 (2018). https://doi.org/10.1103/PhysRevA.97.042704
35. L. Chen, Y.L. Guo, J.J. Jia et al., Absence of a guiding effect and charge transfer in the interaction of keV-energy negative ions with Al_2O_3 nanocapillaries. Phys. Rev. A **84**, 032901 (2011). https://doi.org/10.1103/PhysRevA.84.032901
36. G.Z. Sun, X.M. Chen, W. Jun et al., Interaction of 18-keV O^- ions with Al_2O_3 nanocapillaries. Phys. Rev. A **79**, 052902 (2009). https://doi.org/10.1103/PhysRevA.79.052902
37. A.X. Yang, D.W. Zhou, C.Z. Han et al., Simulation of the dynamical transmission of 100 eV positrons through a conical capillary. Nucl. Instrum. Methods Phys. Res. Sect. B **549**, 165264 (2024). https://doi.org/10.1016/j.nimb.2024.165264
38. D. Tomono, T.M. Kojima, K. Ishida et al., Focusing effect of MeV muon beam with a tapered capillary method. J. Phys. Soc. Jpn. **80**, 044501 (2011). https://doi.org/10.1143/JPSJ.80.044501
39. T.X. Sun, Capillary X-ray lens technology and its applications. Acta Opt. Sin. **42**, 1134002 (2022). https://doi.org/10.3788/AOS202242.1134002. (**in Chinese**)
40. H.Q. Li, S.K. Shao, X.P. Sun et al., Simulation and characterization on tapered monocapillary high-energy X-ray lens with microfocal spot. Acta Opt. Sin. **42**, 1134019 (2022). https://doi.org/10.3788/AOS202242.1134019. (**in Chinese**)
41. B.G. Feng, F. Tao, Y.M. Yang et al., X-ray fluorescence microtomography based on polycapillary-focused X-rays from laboratory source. Nucl. Sci. Tech. **29**, 85 (2018). https://doi.org/10.1007/s41365-018-0417-x
42. T. Nebiki, T. Yamamoto, T. Narusawa et al., Focusing of MeV ion beams by means of tapered glass capillary optics. J. Vac. Sci. Technol. A **21**, 1671–1674 (2003). https://doi.org/10.1116/1.1597889
43. J. Hasegawa, S. Jaiyen, C. Polee et al., Transport mechanism of MeV protons in tapered glass capillaries. J. Appl. Phys. **110**, 044913 (2011). https://doi.org/10.1063/1.3624617
44. S.D. Liu, Y.T. Zhao, Simulations of 1-MeV proton transmission through an insulating conical macrocapillary: Further insight into transmission mechanisms. Nucl. Instrum. Methods Phys. Res. Sect. B **491**, 1–6 (2021). https://doi.org/10.1016/j.nimb.2021.01.011
45. J.F. Ziegler, M.D. Ziegler, J.P. Biersack, SRIM-The stopping and range of ions in matter (2010). Nucl. Instrum. Methods Phys. Res. Sect. B **268**, 1818–1823 (2010). https://doi.org/10.1016/j.nimb.2010.02.091
46. J.F. Han, Z. An, G.Q. Zheng et al., An ion beam facility based on a 3 MV tandetron accelerator in Sichuan University, China. Nucl. Instrum. Methods Phys. Res. Sect. B **418**, 68–73 (2018). https://doi.org/10.1016/j.nimb.2018.01.002
47. M. Schulte-Borchers, M. Döbeli, A.M. Müller et al., Time-of-flight MeV-SIMS with beam induced secondary electron trigger. Nucl. Instrum. Methods Phys. Res. Sect. B **380**, 94–98 (2016). https://doi.org/10.1016/j.nimb.2016.05.011
48. M.J. Simon, Dissertation. ETH Zurich (2013). https://doi.org/10.3929/ETHZ-A-009796626
49. A.Y. Konobeyev, U. Fischer, Y.A. Korovin et al., Evaluation of effective threshold displacement energies and other data required for the calculation of advanced atomic displacement cross-sections. Nucl. Energ. Technol. **3**, 169–175 (2017). https://doi.org/10.1016/j.nucet.2017.08.007